9. OTHER THEORY AND MODELLING STUDIES

F. Serra and J.P. Bizarro (Heads), J. Belo, R. Coelho, J. Ferreira, A. Figueiredo, S. Hacquin, M.E. Manso, P. Rodrigues, F. Salzedas, F. Silva

9.1. INTRODUCTION

This chapter contains information about theoretical and simulation studies on:

- Transport and MHD;
- Non-inductive current drive;
- Modelling of microwave reflectometry measurements.

9.2. STUDIES ON TRANSPORT AND MHD ACTIVITY

9.2.1. Introduction

The activity of this project has been focussed in the following research lines:

- Triggering of neo-classical tearing modes by mode coupling
- Sawtooth and impurity accumulation control in JET Radiative Mantle discharges
- On the sawtooth precursors at the onset of neoclassical tearing modes
- Numerical simulation of sawtooth stabilisation by ICRH driven fast particles for different JET scenarios
- Influence of the position of the ICRH resonant layer over the internal kink mode stability
- Nonlinear dynamics of magnetic islands
- Physics of disruptions

The work related with the first five research lines has been performed under the JET Implementing Agreement and is described in chapter 3.

9.2.2. Nonlinear dynamics of magnetic islands[1]

9.2.2.1. Forced magnetic reconnection

The attainment of high performance tokamak plasma operation and confinement depends strongly on the avoidance of locked modes. Owing to an imperfect alignment of the equilibrium toroidal magnetic field coils, a residual (error-field) static magnetic field with multiple poloidal (m) and toroidal (n) harmonics cannot be avoided. When there is a magnetic surface inside the plasma with an associated safety factor q=m/n (assumed to be tearing stable), the (m,n) component of the error-field may force some reconnection at the q=m/n surface, leading to the growth and saturation of a magnetic island with a given width. For rotating plasmas, the forced reconnection of an otherwise stable mode (in the absence of error-fields) is also associated with a significant drop of the plasma toroidal rotation, and a further amplification of the mode amplitude . This motivated an extensive numerical analysis of the forced reconnection and amplification of stable ohmic tearing modes by external resonant magnetic fields in a large aspect ratio cylindrical geometry (a first approximation to the realistic toroidal geometry) . The numerical code solves the reduced MHD set of equations (9.1-9.4) for the perturbed magnetic flux ($\psi_{(m,n)}$) and plasma vorticity

$$(U_{(m,n)} = -\nabla \times v\big|_{z,(m,n)})$$

together with the equilibrium flux ($\psi_{(0,0)}\equiv\psi_0$) and toroidal plasma rotation frequency ($v_{z,(0,0)}\equiv v_{z0}$) :

$$\frac{\partial \psi_{(m,n)}}{\partial t} = -\eta_0 J_{z,(m,n)} - \vec{v}\cdot\nabla\psi\big|_{(m,n)} \qquad (9.1)$$

$$\rho_0 \frac{\partial U_{(m,n)}}{\partial t} = -\rho_0 \vec{v}\cdot\nabla U_z\big|_{(m,n)} - \vec{B}\cdot\nabla J_z\big|_{(m,n)} + \nu_0 \nabla^2 U_{(m,n)} \qquad (9.2)$$

[1] Work carried out in collaboration with Istituto di Fisica del Plasma.

$$\frac{\partial \psi_0}{\partial t} = -\eta_0 J_{z0} - \vec{v} \cdot \nabla \psi \Big|_{(0,0)} + E_0 \qquad (9.3)$$

$$\rho_0 \frac{\partial v_{z0}}{\partial t} = \vec{J} \times \vec{B} \Big|_{z,(0,0)} - \rho_0 \vec{v} \cdot \nabla v_z \Big|_{(0,0)} + \nu_0 \left(\nabla^2 v_{z0} - \nabla^2 v_{z0,t=0} \right) \qquad (9.4)$$

The subscript 0 denotes equilibrium quantities and ρ, η and ν are the mass density, electrical resistivity and isotropic anomalous viscosity. The E_0 is the equilibrium toroidal magnetic field and the

$$\nabla^2 v_{z0,t=0}$$

term is added to prevent the diffusion of the equilibrium profile in the absence of any magnetic perturbations.

The amplification of the mode contemporary to the halving of the toroidal plasma rotation frequency at the mode's rational surface was observed in the numerical simulations, in agreement with the experimental features of mode amplification (Figures 9.1 and 9.2). Preliminary numerical results also indicate an agreement between the experimentally observed non localised damping of the toroidal rotation profile during the reconnection process (Figure 9.3) and a neoclassical viscous force, arising from the asymmetric plasma equilibria with an helical island, proportional to some power of the poloidal and toroidal magnetic field perturbations. This is shown in Figure 9.4, where the simulated time evolution of the toroidal plasma rotation frequency is shown (with the neoclassical viscous force added to equation (9.4)).

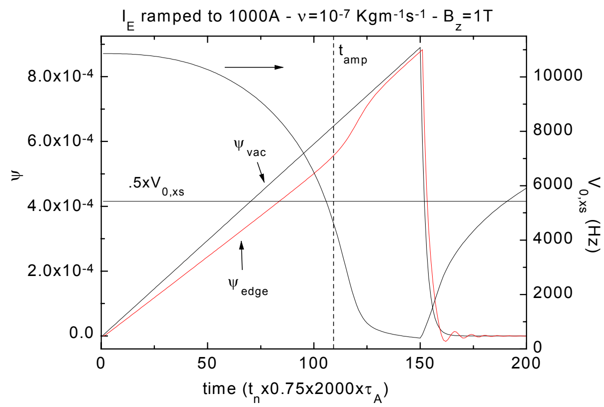

Figure 9.1 – Forced reconnection and amplification (t=t_{amp}) of a stable (2,1) mode, driven by a external ramped resonant helical current. At t=t_{amp}, the toroidal plasma rotation frequency at the rational surface is halved .

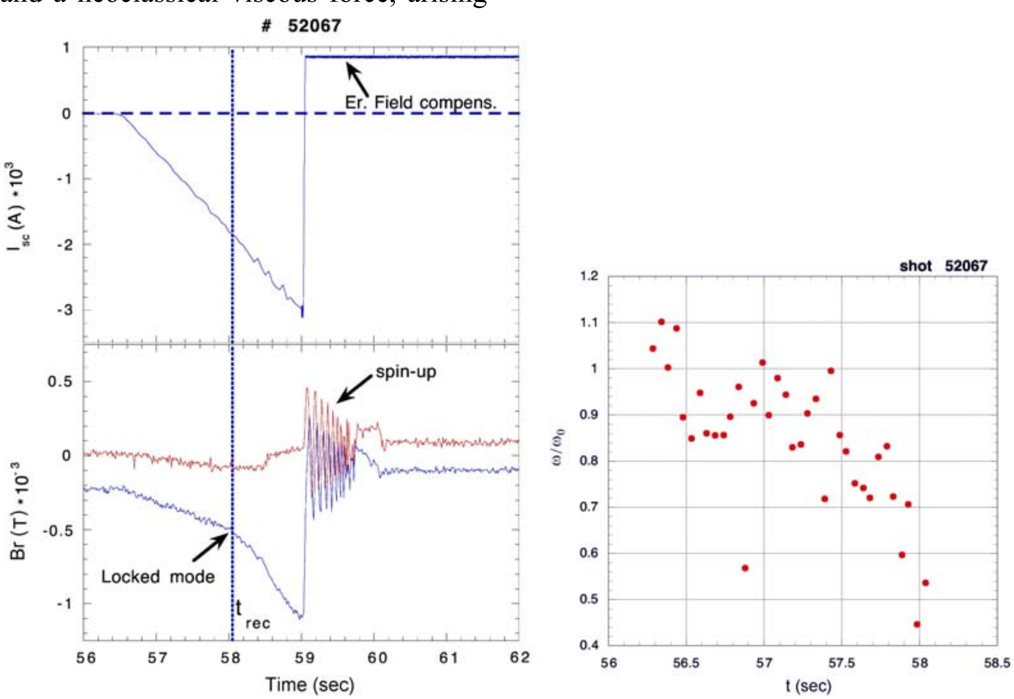

Figure 9.2 – Characteristic experimental results of the mode amplification in a JET discharge. The amplification (left traces) occurs when the toroidal rotation is halved (right figure)

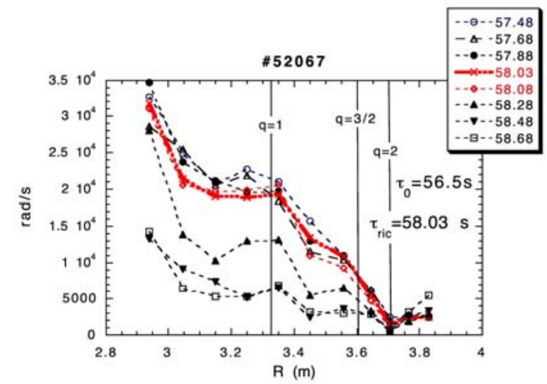

Figure 9.3 - Experimental time evolution of the toroidal angular velocity evidencing a non diffusive behaviour and the presence of non-localised torques

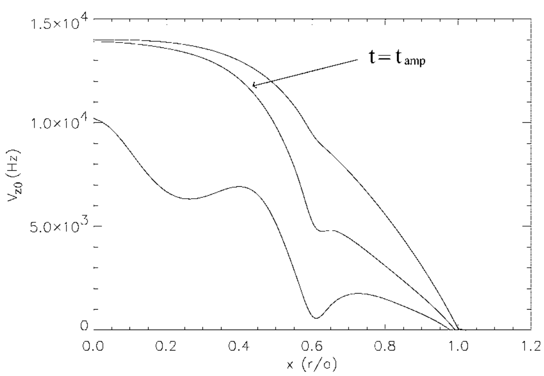

Figure 9.4 – Neoclassical viscous force effect on the time evolution of the toroidal rotation frequency profile (the mode amplification occurs at t=t_{amp}) [3]

In addition from the numerical simulations, important scaling laws for the dependence of the error-field amplification threshold on key plasma parameters (anomalous plasma viscosity-ν, rotation frequency-$V_{0,xs}$) and operational discharge parameters such as the toroidal magnetic field (B_z) where inferred, being summarised below . Although a large toroidal rotation frequency is beneficial since it increases the error-field amplification threshold, for larger operating toroidal magnetic fields, there is a lower limit to maximum tolerable error field since the relative threshold b_{thresh}/B_z scales as $b_{thresh}/B_z \propto B_z^{-0.725}$ (I_{thresh}(A) $\propto V_{0,xs}$, $\propto \nu^{0.43}$, $\propto B_z^{0.275}$).

9.2.2.2. Three wave resonance interaction

The successful control of resistive tearing instabilities must take into consideration the inevitable occurrence of non-linear driven modes, arising from a three wave resonance interaction between tearing modes . In order to investigate the onset and amplification of such non linear driven modes, a multiple helicity numerical code (an extension of the reduced MHD code already available for a single helicity (Eqs. 9.1-9.4)) was used to analyse these modes in the framework of driven forced reconnection. The dynamics of the driven mode is in fact very similar in nature to a forced reconnection process. For typical toroidal plasma rotation profiles smoothly decreasing with the minor radius, the three modes almost satisfy automatically a three wave frequency matching condition, favouring the driven reconnection of a stable mode by the mode coupling interaction with two unstable modes. For low β plasmas, and excluding (1,1) modes, non linear mode coupling was shown to be relevant only for low central shear parabolic safety factor (q) profiles (Figure 9.5), involving a dominant unstable (2,1) mode, a satellite (lower width) unstable (3,2) and a driven (5,3) mode.

These results from the fact that tearing instability at low β for the (3,2) only arises for such safety factor profiles. At high β, when the neo-classical bootstrap current effects play a dominant role, such a constraint on the q-profile vanishes, and non-linear driven mode excitation should be observed more frequently, as long as the two driving modes, for this specific case the (2,1) and (3,2) modes, coexist in the plasma (as is well know, the triggering of (2,1) modes often leads to the cancellation of the (3,2) mode.

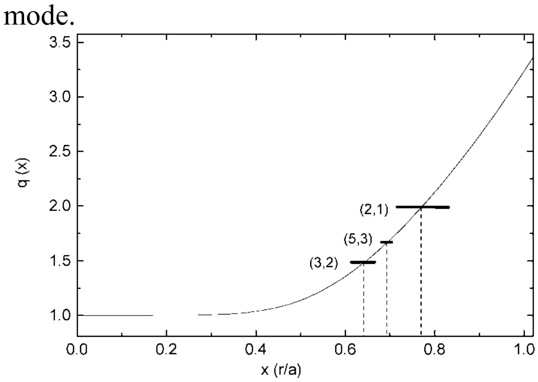

Figure 9.5 – Typical q-profiles unstable to both (2,1) and (3,2) modes. The steady state saturated island widths of the driven (5,3) mode as well as the driving (2,1) and (3,2) modes are also shown (the dashed lines identify the rational surface location of each mode whereas the full thick segments provide an indication of the islands' width)

9.2.2.3. Alternative tearing mode stabilisation methods

(i) Stabilisation by strongly sheared plasma rotation profiles

Analytical and numerical work suggest that the plasma rotation dependence on the minor radius may affect significantly the stability of tearing modes. It has been conjectured that for strongly sheared profiles around the rational surface, where the plasma rotation frequency is zero at the rational surface and positive on both sides, complete mode suppression can be obtained since a $\Delta' < 0$ is obtained ($dW/dt \propto \Delta'$ where W is the island width). The effect of toroidal plasma rotation profiles with such shear on the stability of the modes was therefore analysed numerically by appropriately extending the numerical code to include such an effect. An equilibrium toroidal rotation frequency profile as that given by equation (9.5) was used

$$V_{z0}(x) = V_0 - (V_0 - V_a)\cdot x^3 - a_{\%}V_{0,xs} \cdot e^{-[(x-xs)/\delta h]^2} \qquad (9.5)$$

where $a_{\%}$ is the change in percentage of the rotation frequency at the rational surface ($V_{0,xs}$) and δh is the half width of the depression in the modified rotation frequency profile. A parabolic q-profile with q_0=1, q_a=3.5 ($\Delta' = 8$) and central toroidal rotation frequency V_0=26 kHz were used. The numerical simulations, done with $a_{\%} = 95\%$, show that the shear effects are stabilizing provided the width of the depression in the rotation frequency profile (δW_V_{dep}) is smaller than the island width (Figures 9.6 and 9.7). Additional simulations have shown that for a larger Δ' or a smaller central toroidal rotation frequency, the stabilization effect becomes marginal.

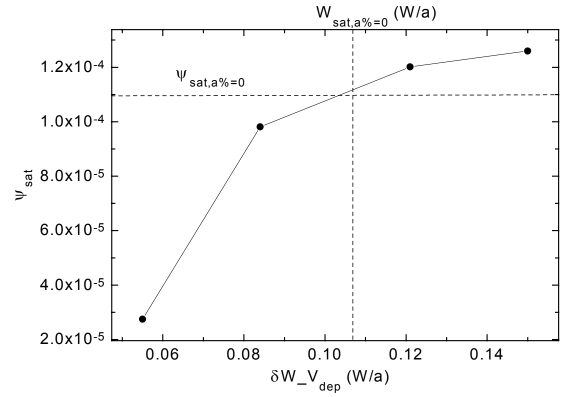

Figure 9.6 – Effect of strong sheared toroidal rotation (Eq.(1)) on the stability of tearing modes

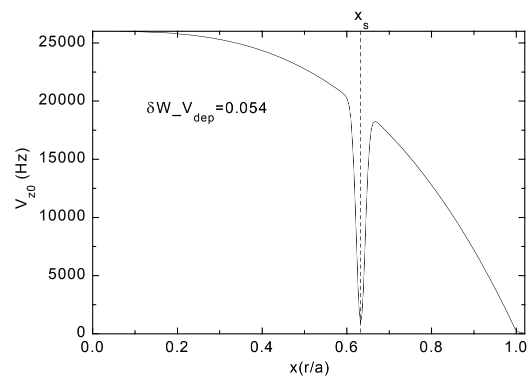

Figure 9.7 – Toroidal rotation frequency profile of the most stabilizing case of figure 9.7

(ii) Stabilisation by static external resonant fields in fast rotating plasmas

The interaction of static external magnetic fields resonant with a particular rotating tearing mode inside the plasma is usually thought to be destabilising when the mode's rotation, under the influence of the external field, is brought to zero . This is based on the assertion that, in steady state, the phase difference between the mode and the external field ($\Delta\phi_E$) is such that $\cos(\Delta\phi_E) > 0$, implying instability. However, such conclusions are drawn from a simplified model for the time evolution of the island width and rotation frequency, based, respectively, on the competition between stabilising and destabilising contributions to the Δ' parameter, and on the competition between the braking electromagnetic torques induced by the external field and the restitution (accelerating) viscous torques originating from the plasma outside the island.

An analysis of the time evolution of the perturbed magnetic field and mode frequency based on the reduced set of MHD equations Eqs. 1-4 is expected to provide a deeper insight on the nature of the interaction. In fact, quite surprisingly, for fast rotating plasmas, a static current is expected to have a stabilising effect, provided the plasma is kept rotating . This is shown in Figures 9.8 and 9.9, where, once the mode is saturated with a finite amplitude, a static current is switched on ($t=t_{IE}$) and a toroidal angular momentum source (neutral beam injection- NBI- for example) is switched on at t=t_{NBI}. On average, the mode amplitude is decreasing, the same happening to the toroidal plasma rotation frequency at the rational surface (Figure 9.8). The decrease in the mode's amplitude (approximately by 70%) is connected to a stabilising phase difference (Figure 9.9). If a momentum source is not supplied to the toroidal rotation, following a continuous decrease of the plasma rotation, the stabilising phase is ultimately lost (ϕ_s becomes positive) and the mode is destabilised (increasing its amplitude significantly).

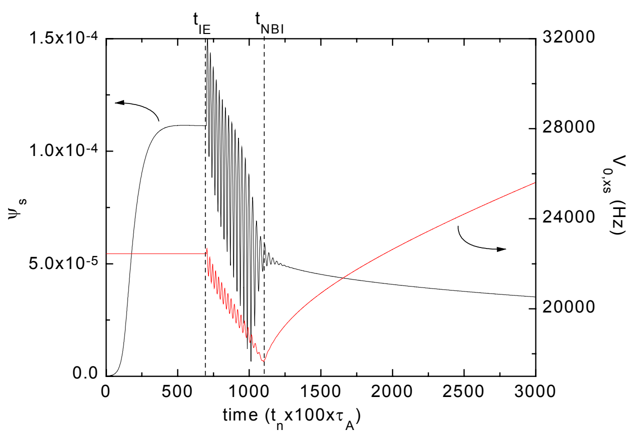

Figure 9.8 – Time evolution of reconnected flux and toroidal rotation frequency at the rational surface. The NBI prevents the $V_{0,xs}$ fall and allows for the consequent stabilization of the mode .

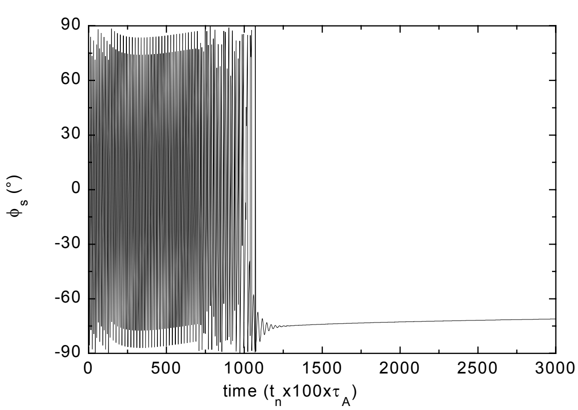

Figure 9.9 – Time evolution of the mode's phase at the rational surface. A stabilizing phase is maintained

9.2.3. Physics of disruptions

Despite disruptions are known since the early days of nuclear fusion research, the cause of the energy quench[2] is still unclear. The available models can only address part of the event and they are static, lacking the capability of predicting the time evolution of the energy quench due to the complexity of this plasma event.

In recent high resolution measurements of the energy quench in RTP (FOM-Institut 'Rijnhuizen') a series of observed phenomena raise the question whether convection is playing a significant role in the fast transport of energy that characterises this event. Two of these observations were : (i) the erosion of the T_e profile in the neighbourhood of the m/n=2/1 mode O-point on the outboard that triggers the well known fast m/n=1/1 T_e erosion (Figure 9.10); (ii) the small decrease of the electron density in the centre of the plasma followed by a large increase (~50%) in the m/n = 2/1 island, also during the same period.

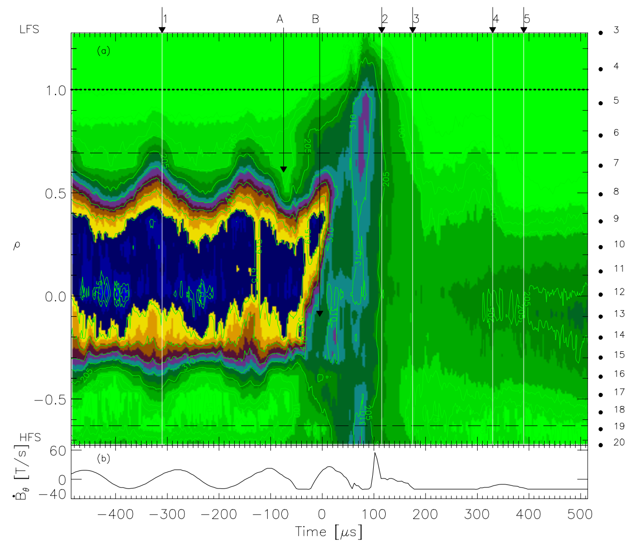

Figure 9.10 - Illustration of a major disruption. (a) Time evolution, with 2 micro seconds time resolution, of the radial temperature profile measured by the ECE radiometer. The position of the channels is indicated at the right. The *horizontal dashed lines indicate the position of the q=2 surface. The dotted line indicates the position of the limiter. Arrows A and B indicate the m/n=2/1, O point erosion. (b) Time derivative of the poloidal magnetic field at the equatorial plane in the low field side and displaced a toroidal angle of 150º from the ECE radiometer.*

Two set of experiments have been planned and proposed for JET and ASDEX Upgrade in order to continue this study in larger tokamaks.

[2] The event where the energy confinement of the plasma is suddenly completely lost.

In the frame of the study of amelioration of disruptions, an experiment is also planned to assess the effect of the ASDEX ECRH system on the recovery of the plasma current (when switched on at the onset of the current quench that follows the energy quench), as observed at RTP.

9.3. STUDIES ON NON-INDUCTIVE CURRENT DRIVE

9.3.1. Introduction

This project has had the usual lines of research:

- Studies on lower-hybrid (LH) current drive (CD);
- Development of kinetic codes to solve the Fokker-Planck (FP) equation.

where the following main activities were carried out:

- Continuation of the writing of a fully 3-D (toroidal plus ripple effects) ray-tracing code;
- Application of beam-tracing techniques for LH wave propagation in tokamaks;
- Improvement of kinetic codes, with interesting developments obtained with path-sum codes.

9.3.2. Beam tracing for LH wave propagation in tokamaks

When modelling LHCD in tokamaks, the interaction between the propagating wave field and the electronic distribution function is usually described with the aid of two coefficients: the damping coefficient, which states how much power is absorbed from the wave field by the electronic population characterised by a given distribution function, and the quasilinear diffusion coefficient, controlling the shape of the distribution function that evolves under the wave-field influence. For a given field mode, the damping coefficient is essentially related with the first derivative of the distribution function at that mode phase velocity. On the other hand, the quasilinear diffusion coefficient value for a given electron velocity vector is proportional to the weighted sum of the squared field amplitude for all modes matching the resonance condition, being the weighting factors given by the squared cosine of the angle between the phase-velocity vector and the magnetic field. Therefore, the computation over each flux surface of the squared field-amplitude spectral distribution, in terms of the refraction index component parallel to the magnetic field, $N_{\|}$, establishes itself as a key step in any LHCD modelling procedure.

For the LH range of frequencies, the standard method to obtain such spectral distributions, and from them the quasilinear diffusion coefficient, is deeply reliant on the geometric optics (GO) approximation and ray-tracing techniques. However, the acknowledgment of several limitations intrinsic to conventional GO, ranging from poor numerical efficiency to its failure to properly account for some wave effects like diffraction, have pushed the need for more detailed descriptions of the LH wave-field propagation to be developed. Due to the smallness of the LH wavelength, full-wave calculations in toroidal geometry present still a daunting challenge and, therefore, an intermediate asymptotic approximation has been sought in the form of a paraxial WKB (pWKB) approximation. While retaining a GO description along the group-velocity direction, the pWKB approximation effectively accounts for the wave properties in the direction transverse to it, enabling one to assess how diffraction effects may contribute to the broadening of the launched LH spectra.

Unlike GO, where the squared field amplitude for each mode is obtained without the call for explicit field construction, the pWKB approach provides the explicit electrostatic potential $\Phi(u,v,\tau)$ in the so-called reference-ray frame $\{u,v,\tau\}$, built around the reference-ray trajectory (u = v = 0), together with rules granting coordinate conversion between the reference-ray frame and the laboratory (or tokamak) frame $\{r,\theta,\phi\}$ (with r being the radial distance to the magnetic axis, and θ and ϕ the poloidal and toroidal angles, respectively). Once the electrostatic potential has been computed, by integrating in τ a system of 17 non-linearly coupled differential equations, it must be evaluated over a set of flux surfaces and then Fourier analysed in the angular variables. The momentum variables, canonically conjugated to the angular variables considered, and in which the spectral distribution is expressed for the time being, must be related to the magnetic-field vector in every point of each flux surface, allowing one to compute the value of $N_{\|}$ associated with each field mode. Since magnetic-field lines do not cross flux surfaces, there is no need to compute spectral distributions along a radial momentum variable, and therefore the Fourier-analysis effort is reduced to two-dimensional fast Fourier transforms (FFT), instead of a full three-dimensional analysis, which would be extremely demanding in computational resources.

The procedure outlined above presents three main problems, which were successfully addressed and solved. The first one, which is related to the transformation rules between the reference-ray and the tokamak coordinate sets, reflects the fact that, although the transformation from $\{u,v,\tau\}$ to $\{r,\theta,\phi\}$ is a one-to-one correspondence, the reverse is not. In order to assign a single point, in the reference-ray frame, to every point in the tokamak frame, the concept of constant-τ surfaces had to be developed. These constant-τ surfaces are indeed mappings, at different values of the integration parameter τ, of the surface over which the initial distribution of the electrostatic potential $\Phi_0(u,v) = \Phi(u,v,\tau = 0)$ is given, and the evolution of its geometry has been modelled with the aid of 6 additional differential equations, together with proper initial conditions. The second problem has to do with the singular behaviour, near the origin $r = 0$, of the tokamak coordinate set. The standard way to handle this issue involves the change to a coordinate set with non-vanishing Jacobian, like the set $\{R,z,\phi\}$, where R is the distance to the tokamak axis, z is the distance to the equatorial plane and ϕ remains the toroidal angle. However, such coordinate set does not allow a simple description for the $\tau = 0$ surface, which must be expressed as a linear relation of the chosen coordinates. The solution was found by introducing a new curvilinear coordinate set, based on elliptic cylindrical coordinates, which is able to suppress the ill behaviour of singularities whilst still allowing for simple descriptions of initial conditions. At last, the angular variables used to describe the field distribution over each flux surface had also to be redefined in order to turn $N_{||}$ into a flux function, which is far from being a straightforward task for toroidal magnetic equilibria.

After having successfully solved the above mentioned problems, the squared field-amplitude spectral distribution in $N_{||}$ as a function of the flux-surface radius ρ was computed (as depicetd in Figure 9.11 for TRIAM-1M), making possible further developments leading to the calculation of power deposition profiles, which are essential for LHCD modelling.

9.3.3. Path-sum codes for FP equations

The FP equation, which is one of the mainstays in kinetic theory, is fundamental in CD modelling of fusion plasmas using rf power, such as electron-cyclotron (EC) and LH waves. For the solution of the more realistic two-dimensional (2-D) models that have been developed to study LHCD and ECCD,

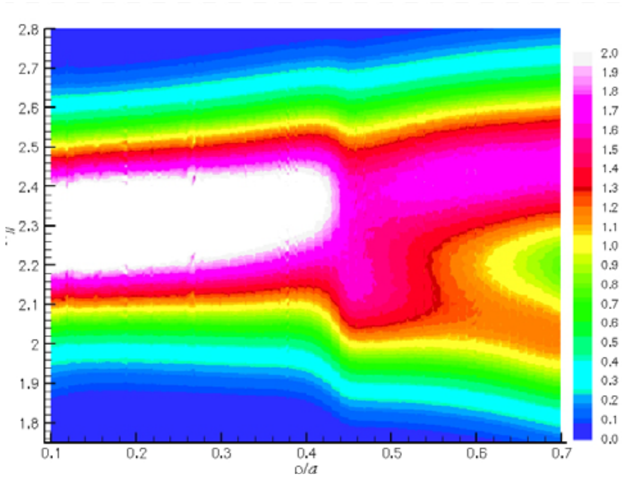

Figure 9.11 – Squared field-amplitude $E^*E(\rho/a,\ N_{||})$ as a function of both the refraction index component parallel to the magnetic field and the flux-surface radius ρ, normalized to the tokamak minor radius a, for a launched gaussian beam centred at $N_{||} = 2$.

there is no recourse other than to resort to some kind of numerical method, as analytical solutions do not abound, whereas finding solutions for specific models as complex as these might be a dead-end road. The most widespread numerical approach consists in directly solving the FP equation by means of finite differences. Still, alternative approaches such as the use of Monte Carlo and propagators have found increased acceptance, as they are known to offer a very simple and clear picture of the kinetics involved and lead, moreover, to a straightforward numerical implementation. Of these, the use of Gaussian short-time propagators to numerically evaluate solutions to FP equations as path sums has been gaining some interest as a valuable alternative to Monte Carlo, over which they have advantages both in terms of accuracy and computational efficiency. However, path-sum schemes (just as, for that matter, Monte Carlo) still face some quite challenging problems when compared to the finite-difference approach. This is especially true concerning the computational efficiency of 2-D calculations, owing to time-step restrictions and concomitant constraints on grid spacing (which implies the handling of very large propagator matrices).

In relation to the application of propagators to the solution of FP models for LHCD and ECCD studies undertaken, the appropriateness of the boundary conditions, whose importance is well known for this type of problems, has been further improved, in particular that pertaining to the external boundary and some of the internal ones as well. To this end some approximations were proposed and tested to give good results for situations where finding the exact analytical form of the bounded propagator (at least with the known techniques used for propagators) would be excessively daunting, if not impossible to tackle. Moreover, new and improved methods were developed with a view to a more efficient computation of the non-negligible elements of the 2D propagator matrix by reducing the number of mistrials.

The propagator implementation of the 2D model of LHCD was taken a step forward to higher, yet moderate, values of the rf diffusion coefficient than before, extending up to $D_{rf} \leq 1$, a standard value in these studies. To meet this goal, a special technique had to be created with which to allocate more efficiently the computer resources to the two main regions: the resonant and the non-resonant ones. As the propagator formulation previously developed reveals, the former region places more stringent conditions on both the time step and the cell width than the latter. Accordingly, with this technique the propagator matrix for the resonant region is first computed with its appropriate time step and grid, and then used to determine the propagator matrix for a larger time step. Afterwards the resulting propagator is converted to a larger cell grid where the propagator matrix for the non-resonant region is also determined using the larger time step. These two large parameters (time step and cell width) are selected to be more suitable for the conditions reigning in the less severe non-resonant region. At this point the problem is totally converted to the new large time step and grid, where the evolution of the entire system is followed from then on. The results of the numerical implementation are not only better than previously obtained with the propagator approach, but also in a very reasonably good agreement with the corresponding finite-difference solutions. Moreover, and as a spin-off, they are achieved using much shorter CPU times. Unfortunately for higher values of D_{rf} the restrictions imposed by the time-step and cell-width criteria point towards the need to handle excessively and increasingly large propagator matrices such that from the computational stance it rapidly becomes an unacceptable burden to bear. Still, this is a more acute problem for LH than EC waves given the strong parallel diffusion induced by the former compared to perpendicular diffusion of the latter.

For the first time the limiting situation in ECCD where an extremely high power rf wave such that $D_{rf} \to \infty$ is used was treated in this approach. It should be remarked that solving such a problem represents an important breakthrough for path sums in modeling rf current drive as, until this was achieved, it seemed out of reach of propagators – even though it was already solved by finite differences, with recourse to the same principles used now in propagators – given that, not only is such a D_{rf} not moderate by any standards (a limitation the previously reported studies appeared to impose), but it is not even finite. The numerical implementation demonstrated that propagators are capable of achieving good results also in this severe situation (Figure 9.12), showing that this approach is indeed appropriate at least for low-to-moderate and extremely high rf powers.

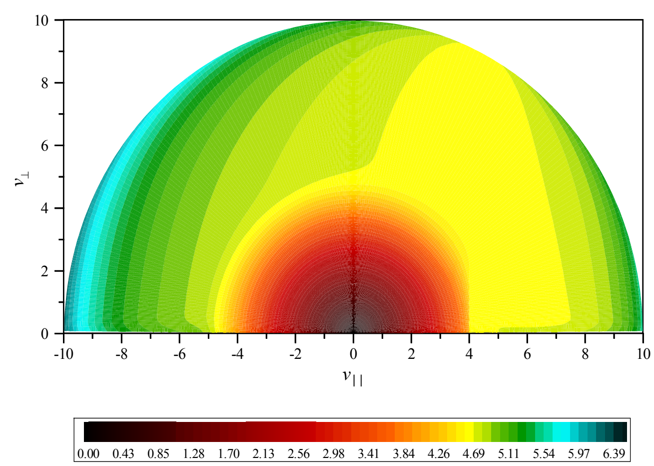

Figure 9.12 - Contour plot of the steady-state electron distribution function $f_{st}(v_{||},v_\perp,t \to \infty)$ for ECCD when the rf quasilinear diffusion coefficient obeys $D_{rf} \to \infty$. The contour levels are for constant values of the quantitity $\{-2\ln[(2\pi)^{3/2} f_{st}(v_{||},v_\perp,t \to \infty)]\}^{1/2}$, which would yield equally spaced circles for a Maxwellian distribution.

9.4. MODELLING OF REFLECTOMETRY EXPERIMENTS

9.4.1. Introduction

The following main activities have been made in 2001[3]:

- Development of 2D wave propagation models to characterize the wave scattering at micro and macro turbulence;
- Development of a 2D code for broadband reflectometry that replicates the main characteristics of the reflectometry diagnostic on ASDEX Upgrade (detection, sweeping, data analysis);
- Simulation of profile changes occurring during type I ELMs and when a rotating magnetic island is present.
- Identification of the modes signatures on the broadband signals

9.4.2. Modelling of non-coherent density fluctuations

9.4.2.1. Model of density fluctuations

Turbulent phenomena in tokamaks induce density fluctuations that are superimposed to the average density profile. In the 2D case, the density profile can be then written as follows:

$$n_e(x,y) = \langle n_e(x,y) \rangle + \delta n_e(x,y) \tag{9.6}$$

where x and y are respectively radial and poloidal coordinates. Turbulence measurements performed in Tore Supra have shown that the density fluctuations present k-spectrum components until 10 - 20 cm^{-1}. Then we assume that the density fluctuations can be decomposed as Fourier series:

$$\delta n_e(x,y) = \sum_{k_x=-n}^{+n} \sum_{k_y=-m}^{+m} a(k_x,k_y) \cos\left(k_x x + k_y y + \varphi(k_x,k_y)\right) \tag{9.7}$$

where k_x and k_y represent the radial and poloidal components of the spectrum and $\varphi(k_x,k_y)$ is a random phase. The amplitude spectrum $S(k_x,k_y)$ of density fluctuations is thus defined by the coefficients $a(k_x,k_y)$. Depending on the random choice of the phase terms $\varphi(k_x,k_y)$, we can note that an infinity of solutions for the density fluctuations gives the same spectrum. Consequently, the study of the effect of a given fluctuation spectrum should require a large number of cases to get a statistical response. A displacement of the density fluctuations with respect to time (for instance to simulate the poloidal rotation of the turbulence) can also be simulated by the code. Just note that the spectrum changes in the presence of a velocity shear. In the results depicted in the following, an experimental-like spectrum (i.e. plateau for k < 4 cm^{-1} and k^{-3} decreasing for 4 cm^{-1} < k < 15 cm^{-1}) has been input in our code.

9.4.2.2. Broadband frequency reflectometry simulation

Simulation of broadband reflectometry experiments where frequency sweeping time ≥ 20 µs imposes a large number of iterations resulting in long computing times for 2D codes. From 1D simulations we show in the case of a frozen density profile that a shorter sweeping time can be used without any significant effect on the phase of the reflected signal. This is illustrated in Figure 9.13 for two different sweeping times (20 µs and 50 ns) in the presence of a high level of turbulence (10% normalized to the maximum density). The amplitude of thereflected signal presents large variations for the short sweeping time (50 ns) whereas it is almost unperturbed for a sweeping time of 20 µs. However, we can notice that the group delay profile determined from a sliding normalised FFT technique remains surprisingly identical whatever the sweeping time. Consequently, we use in the following 2D simulations a sweeping time of 50 ns assuming that it remains relevant to study the fluctuation effects on the time of flight (but not on the amplitude of reflected signal).

Figure 9.14 presents contour plots of the electric field (at a given time during the frequency sweeping) without density fluctuations and in the presence of density fluctuations with a level of 10% are compared, showing the wave scattering induced by such fluctuations. The effect on the time of flight is exemplified in Figure 9.15, where a comparative study is made for density fluctuations of 3%, 5% and 10%. In each case, 5 random choices of phase values needed to define the density fluctuations have been considered. The perturbations remain small for 3 % (0.1 - 0.2 ns) and will not affect significantly the profile reconstruction. For a level of 10%, the time of flight perturbations can be extremely strong (until 1 ns) which will prevent the correct density profile reconstruction.

[3] In collaboration with the University of Nancy, France.

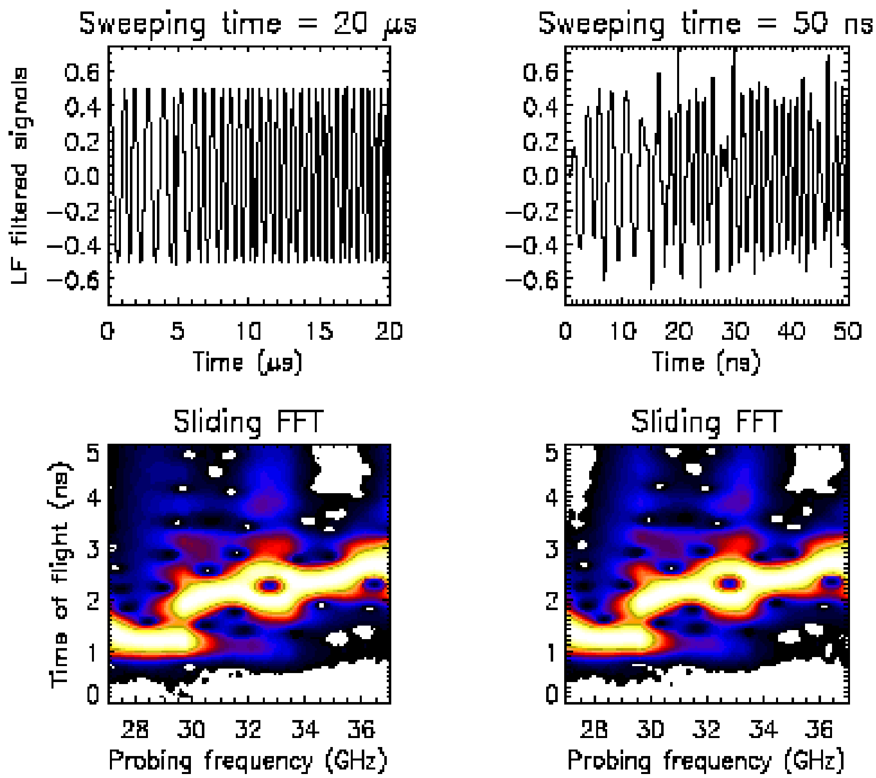

Figure 9.13 – Low frequency filtered signals (top) from 1D code and corresponding sliding FFT curves (bottom) in the presence of non-coherent density fluctuations (level of 10%)

A reduction of the reflectometry signal perturbations is generally noticed during improved confinement regimes (H mode, ITB). Two hypotheses are suggested to explain this reduction, namely a local steepening of the density profile and a modification of the density fluctuation spectrum. The effect of the steepening of the density profile. Using the same density fluctuations of 10 %, we made a simulation for two types of density profile (Figure 9.16). As expected the time of flight profile shows a reduction of the perturbations for the steeper profile, thus confirming the influence of the density gradient on the signal perturbations (Figure 9.17).

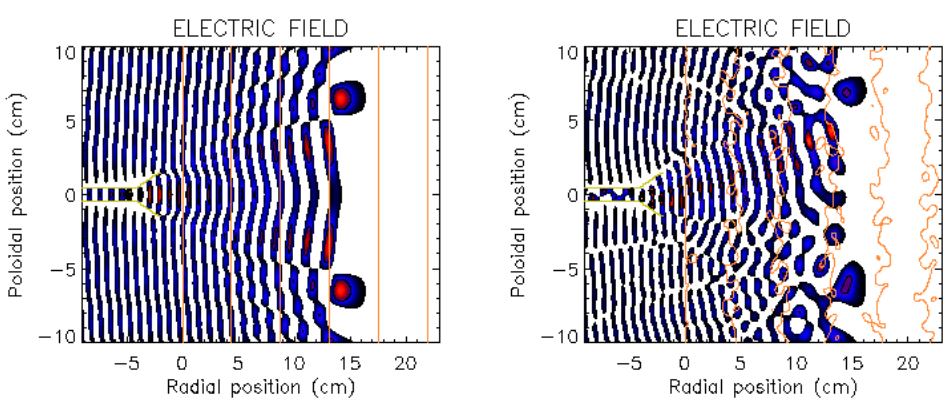

Figure 9.14 – Electric filed contour plot from 2D code without density fluctuation (on left) and in the presence of non-coherent density fluctuations with level of 10% (on right).

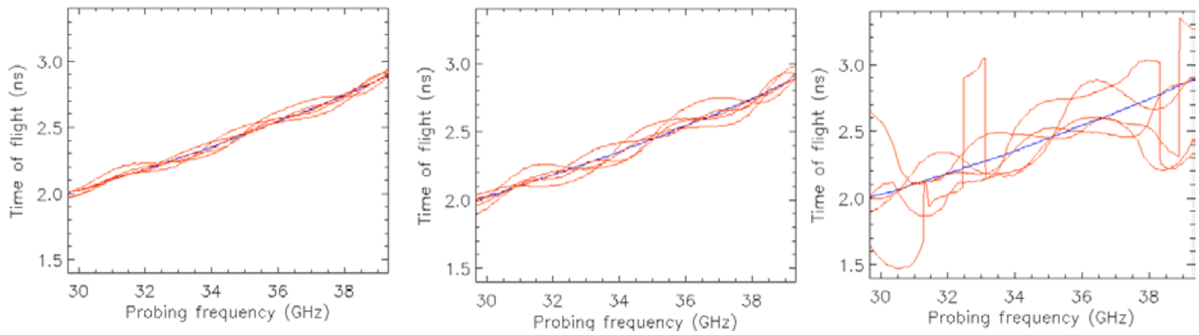

Figure 9.15 - Perturbations on the time of flight in the presence of non-coherent density fluctuations (respectively for 3,5 and 10 %)

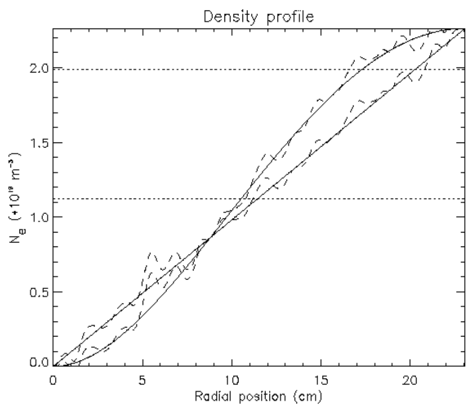

Figure 9.16 – Linear and peaked density profiles with superposition of the same density fluctuations (the two vertical lines represent the probed region)

9.4.2.3. Fixed frequency reflectometry simulation

In this section the effect of poloidal rotation of the turbulence in fixed-frequency reflectometry is studied. Simulations in the 2D case are limited by very demanding computing times. As an example, for the numerical box used in these simulations (30 and 20 cm in radial and poloidal directions), the study of wave propagation during 500 ns requires 20 hours of computing time (on PC computer - AMD Athlon 850 MHz – RAM 256 Mb). Thus for reasonable computing times, the time range for physical phenomena study remains generally too small to see significant phenomena occurring in fusion plasmas. For instance, measurements of poloidal rotation of the turbulence suggest velocities in the order of few km/s. Observation times at least in μs range should be then considered to study the effect of poloidal rotation. Preliminary results suggest that the rotation velocity can be increased without qualitative change (that must be confirmed with additional simulations). Consequently, in order to reduce the computing time the velocity of turbulence rotation has been largely increased in the following simulation. Simulating the poloidal rotation of the turbulence (5% of amplitude with velocity shear in radial direction), we analyse the reflectometer response when the rotation velocity increases as occurs during the formation of transport barriers (Figure 9.18 on left). As seen in experiments, the spectral analyse of the reflected signal highlights the high frequency shift due to the velocity increasing (Figure 9.17 on right). More simulations should be done in the future to interpret Doppler reflectometry experiments.

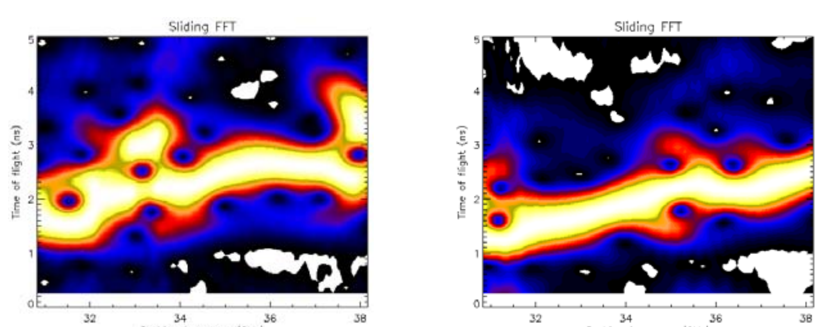

Figure 9.17 - Reduction of time of flight perturbations for steeper profile

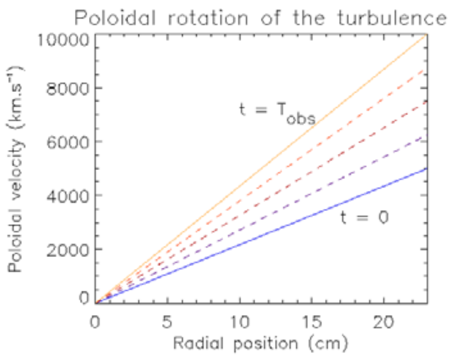

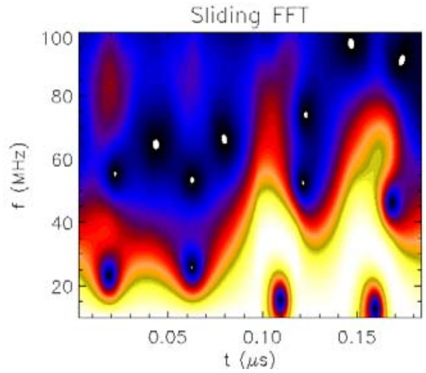

Figure 9.18 - Effect of poloidal rotation of the turbulence on fixed-frequency reflectometry measurements (Note that unrealistic velocities have been considered to reduce the computing time)

9.4.3. 2D FDTD Maxwell code-application to the study of localized quasi-coherent modes in density measurements using o-mode broadband reflectometry

9.4.3.1. Description

In order to interpret correctly the variations of the phase derivative we have developed a 2D finite-difference time-domain (FDTD) Maxwell code suited to describe profile measurements[4]. The simulations permit to obtain the signatures of localized plasma modes and to test some assumptions on the origin of the density profile perturbations observed in the reflectometry experiments on ASDEX Upgrade. Two cases were analyzed: (i) in the first simulation we consider a simple model which shows that density deformations can conduct to destructive interference; (ii) in the second set of simulations the effects of Gaussian perturbations, both in the phase derivatives and the the reconstructed density profiles, are studied.

9.4.3.2. Simulations

In all of the following simulations, the plasma was probed in the K_a microwave band, covering a density range $[1\text{-}2]\times10^{19}$ m^{-3}, by linearly sweeping the frequency of the probing signal from 30 GHz up to 40 GHz. We consider a single horn antenna for emission and reception and as used in the reflectometer diagnostic on ASDEX Upgrade. The reflectometric signal was recovered with an homodyne detection scheme.

9.4.3.3. Double density gradient interference

In the first case, the antenna beam illuminates a plasma with two regions (1 and 2) having different linear density gradients (Figure 9.19). This simulates in a simple way situations where plasma perturbations (e.g. due to a magnetic mode) originate local flattening of the profile. The gap between the cut-off layers is calculated to cause a destructive interference for a given frequency. A 1D model based on Airy functions can be used to give an order of magnitude of the spatial variation involved: the electric fields corresponding to the two simulated gradients, for a frequency f = 32.5 GHz, appearing in (Figure 9.20), are in opposition at x = 17.15 λ_{40GHz} in a gap of ~ between cut-off layers. The detected simulation signal, A(t) cos[φ(t)], presents a destructive interference around 32.5 GHz resulting in a decrease of amplitude (Figure 9.21).The signal does not drop to zero as the 1D model suggests since there are other 2D effects that also play a role.

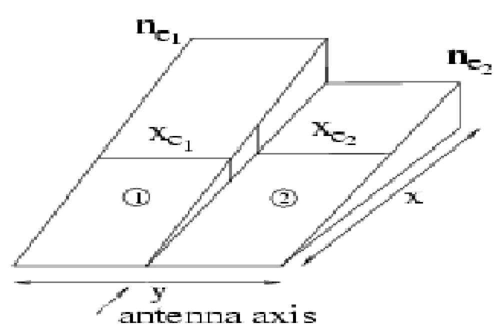

Figure 9.19 - Two density gradients chosen in order to create a destructive interference

[4] Annual Report 2000.

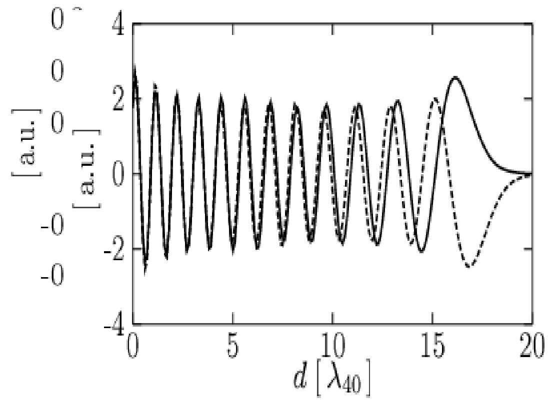

Figure 9.20 - Field amplitudes annulling 16.6λ_{40}

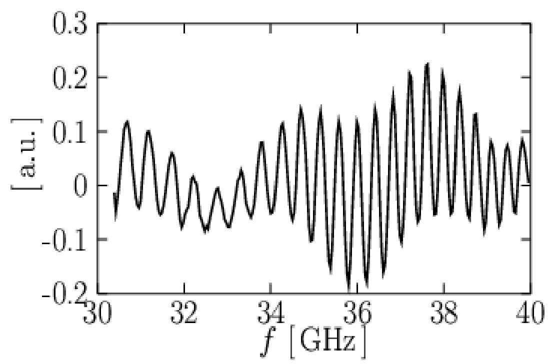

Figure 9.21 – Signal showing destructive interference 32.5 GHz

The associated perturbation in the phase derivative can be observed in Figure 9.22, where the doted lines show the theoretical phase derivatives for each half of the density profile.

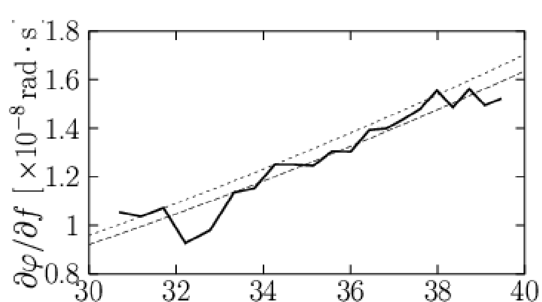

Figure 9.22 – Jump in $\partial\varphi/\partial f$ due to destructive interference

9.4.3.4. Gaussian perturbations

9.4.3.4.1. Fixed radial Gaussian

A Gaussian perturbation,

$$\delta n_e = a_f \exp\left[-(x-x_f)^2/w_x^2\right] \exp\left[-(y-y_f)^2/w_y^2\right] \tag{9.8}$$

is placed in front of the emission/reception antenna, having its center $(x_f, y_f) = (x_{c35}, 0)$ aligned with the antenna axis, where x_{c35} is the cut-off position for f = 35 GHz.

For the chosen simulation parameters, the limit between feeble and strong amplitude, given by $(2\pi L_{40GHz}/\lambda_{40GHz})^{-2/3}$, is 3.3%. With an amplitude of a_f = -3%, the imposed perturbation is at this limit, reinforcing the response while keeping non-linear effects low. The spatial extention of the perturbation, fixed at $w_x = w_y = 3\lambda_{40GHz}$ is wide enough to ensure a quasi-spatial regime (with negligible spectral effects). The resulting phase derivative appears in Figure 9.23. It can be noticed that the phase derivative deviates from the unperturbed case, having an higher value almost throughout the sweep.

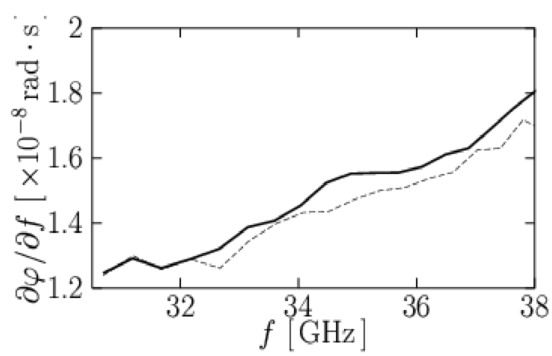

Figure 9.23 - $\partial\varphi/\partial f$ due to fixed radial Gaussian

9.4.3.4.2. Poloidally moving Gaussian

Taking the Gaussian perturbation used above we moved it poloidally along an iso-density line, (x_{c35}, y(t)), where x_{c35} is the cut-off position for f = 35 GHz. The perturbation starts moving synchronously with the frequency sweep, passing in front of the antenna at mid-sweep. The effect of the traveling Gaussian results in a noticeable well-localized decrease in the signal amplitude (Figure 9.24). The influence of the moving Gaussian in the phase derivative (Figure 9.25) is observed from ~ 33 GHz

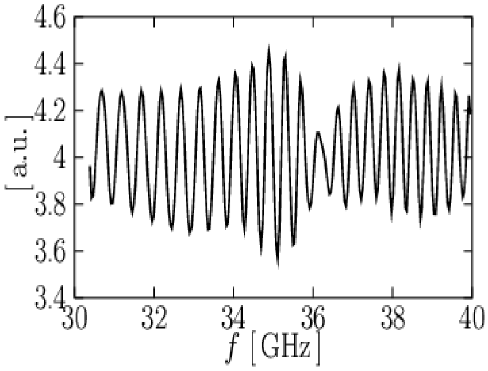

Figure 9.24 – Reflectometric signal for a moving Gaussian

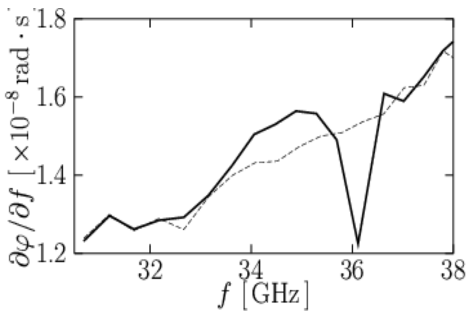

Figure 9.25 - ∂φ/∂f for a moving Gaussian

to ~ 37 GHz. The strong decrease in its value, around 36 GHz, correlates well with the amplitude decrease observed in the signal.

9.4.3.4.3. Fixed lateral Gaussian

The same Gaussian perturbation used in the previous simulations was now fixed laterally to the antenna axis at (x_{c35}, -2.48 λ_{40}), the same position where the decrease of amplitude and phase occurs with the moving Gaussian. In the reflectometric signal (Figure 9.26), a strong decrease in the amplitude of the signal occurs, extending widely across the sweep and reaching it minimum at 38 GHz. This decrease in amplitude corresponds to a moderate decrease in phase derivative, except around 38 GHz where a strong drop in phase derivative is observed (Figure 9.27).

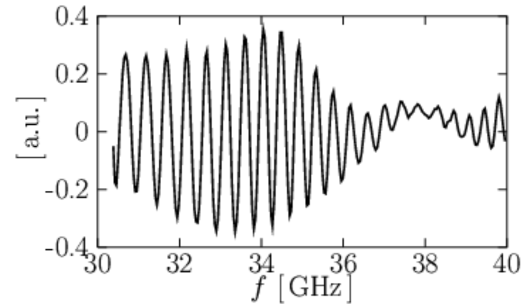

Figure 9.26 – Reflectometric signal for lateral fixed Gaussian

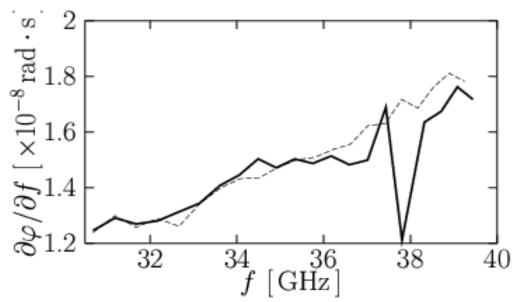

Figure 9. 27 - ∂φ/∂f for a lateral fixed Gaussian

9.4.3.5. Profile reconstruction

To reconstruct the density profiles, the initial part of the phase derivatives (under the first swept frequency) were calculated from the analytical expression for a linear density profile $\partial\varphi/\partial f = 8\pi(x_M-x_m)/c(f/f_M)^2$.

The complete phase derivative is then Abel inverted to obtain the distance d(f) of the reflecting layers. The density profiles for the simulations with Gaussian perturbations are presented in Figures 9.28, to 9.30. The doted lines correspond to the reconstructed unperturbed profiles.

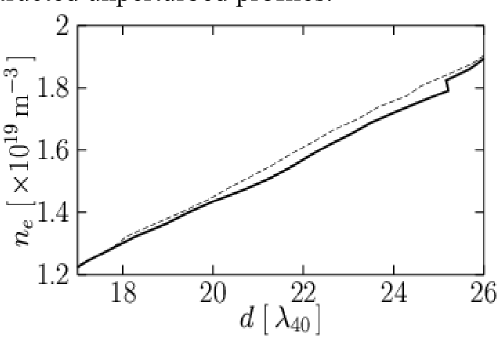

Figure 9.28 – Profile – radial Gaussian

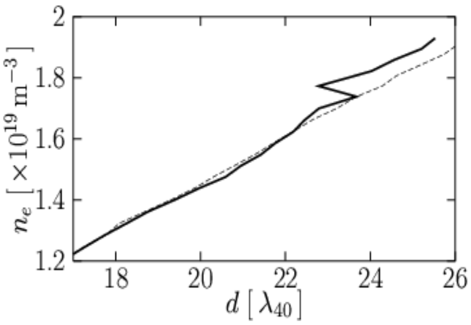

Figure 9.29 – Profile – moving Gaussian

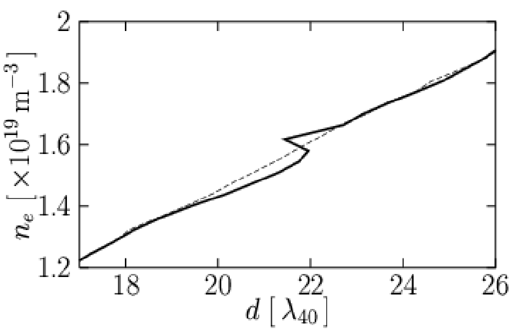

Figure 9.30 – Profile – lateral Gaussian

9.4.3.6. Improvements on the 2D FDTD Maxwell code

Together with the physical studies and simulations important work on the 2D code was done. The code has been entirely rewritten and differs from the former by the use of dynamic allocation of memory. During its writing, a general cleaning took place and some of the procedures were optimized. In what execution speed is concerned, a dramatic improvement was obtained. The increase in speed has allowed us to double the number of points per wavelength, thus decreasing the phase error by a factor of 7.

The improvements in the code and the benchmarking performed lead also to the conclusion that the performance could greatly improve with the implementation of unidirectional signal injection conditions. The implementation of unidirectional injection to the FDTD Maxwell code based on the procedure used in the FDTD Wave Equation code has started and has been given high priority.

During the benchmarking tests it was noticed that the absorbing boundary conditions used may have a significant reflection coefficient which may be particularly important at the back of the emission/receiving waveguide due to the closeness of the boundary to the emission point. The use of a Perfectly Matched Layer (PML) to close the waveguide should obviate the border reflected component in the guide.

An alternative way of referencing the memory positions which resulted in a improvement of in speed was tested. It was also tested a new way of defining the waveguide and antenna which should offer an easier and more flexible way of modeling metallic structures (o-mode). This proved also to be faster for the case tested. This two possible improvements are independent and should be used simultaneously. They are being incorporated in the main code.